ELSEVIER

Contents lists available at ScienceDirect

# Materials Science & Engineering A

journal homepage: www.elsevier.com/locate/msea





# Measuring fatigue crack growth using microscale specimens: Si-modified Inconel 939 alloy processed by laser powder bed fusion additive manufacturing

M.H. Shahini <sup>a,1</sup>, Ali Kaveh <sup>a,1</sup>, Bin Zhang <sup>a</sup>, Hamed Ghadimi <sup>a</sup>, S. Guo <sup>a</sup>, C. Zeng <sup>b</sup>, W.J. Meng <sup>a,\*</sup>

### ABSTRACT

Quantitative assessment of fatigue crack growth (FCG) in a Si-modified Inconel 939 alloy, processed by laser powder bed fusion additive manufacturing (L-PBF AM), was conducted through cyclic bending of pre-notched cantilevers with a characteristic cross-sectional dimension of  $25 \, \mu m \times 25 \, \mu m$ . To the best of our knowledge, this work is the first to show that cyclic bending of such pre-notched microscale cantilevers can sense both the threshold regime and the Paris-law regime of FCG quantitatively, despite the small specimen size. The deliberate fabrication of such microscale test specimens enables control of the direction of fatigue crack propagation with respect to a given microstructure, while avoiding the inclusion of volumetric defects within the test volume. Significant differences in FCG behavior were observed when the direction of crack propagation was switched from being parallel to the AM build direction to being perpendicular to it. The present work demonstrates the efficacy of FCG assessment using microscale specimens, which can enhance our understanding of the influence of a given microstructure on crack growth behavior.

# 1. Introduction

Metal additive manufacturing (AM) has been intensely studied over the past two decades [1]. Application of additively manufactured metal parts has been explored by wide ranging industrial sectors, including automotive, aerospace, medical, building and construction, oil and gas [2]. Laser- and electron beam-based AM techniques have been shown to be prone to produce metal parts containing various volumetric defects, which negatively impact part durability [3]. As durability is critical to whether AM metal parts can be safely employed in load-bearing applications, fatigue life assessment of AM metal parts has continued to be a research focus [4,5].

Significant research efforts have been devoted to fatigue of AM metal parts [6]. Many stress – cycle (S-N) and fatigue crack growth (FCG) measurements have been reported or reviewed in the literature [7-9]. Anisotropy of fatigue response of AM metal parts to cyclic loading has been reported. For laser-based AM processes, e.g., laser powder bed fusion (L-PBF), the fatigue performance of so-fabricated metal parts in response to uniaxial cyclic loading has been shown to depend on the orientation of loading axis with respect to the specimen build direction (BD) [10]. The general explanation given for the observed anisotropic fatigue performance of AM metal parts cites the anisotropic

solidification microstructure due to the high cooling rates and the high directionality of heat transfer, as well as the anisotropic nature of defects particular to the L-PBF process [11]. It should be noted that, even with the high cooling rates and highly directional heat transfer typical of laser-based AM, the directionality of microstructure and defects within the metal parts is not perfect, e.g., the long axes of the typically observed columnar grains are not perfectly aligned but rather show a distribution. Furthermore, the AM process typically generates numerous anisotropic volumetric defects within such metal parts [12].

Cyclic loading experiments conducted on AM metal parts, as reported in the present literature, have been carried out at the macroscopic scale, following established protocols for measuring either total fatigue performance (S – N curves) [13] or fatigue crack growth rate (FCGR) [14]. As the characteristic specimen size for such measurements is typically larger than several mm, exceeding the typical dimension of the microstructure or defects within AM metal parts by orders of magnitude, measured S – N curves or FCGR curves necessarily represent a response averaged over numerous differently oriented microstructural domains and influenced by the numerous anisotropic volumetric defects present within the test specimen volume. This type of volumetric averaging leads to contradictory statements in the literature, with some observing a dependence of fatigue performance on the orientation of

<sup>&</sup>lt;sup>a</sup> Department of Mechanical Engineering, Louisiana State University, Baton Rouge, LA, 70803, USA

<sup>&</sup>lt;sup>b</sup> Department of Mechanical Engineering, Southern University, Baton Rouge, LA, 70807, USA

 $<sup>^{\</sup>star}$  Corresponding author.

E-mail address: wmeng1@lsu.edu (W.J. Meng).

<sup>&</sup>lt;sup>1</sup> Authors who contributed equally to this work.

loading axis with respect to BD [10] and others stating no significant difference in fatigue behavior with respect to BD [15,16]. In the latter case, it was noted that the presence of built-in defects can exert a stronger influence than the difference in microstructure due to BD change [15]. A recent work showed differences in measured FCGR in electron beam AM alloy specimens containing mesoscale spatial regions with distinctly different microstructures. While the characteristic microstructural dimension is sub-mm, the FCGR measurement was still conducted at the macroscopic scale [17]. For laser or electron beam AM parts, conducting FCG measurements in microscale specimens offers two advantages, 1) a microscale test specimen can be fabricated such that it contains no volumetric defects, thus eliminating their significant and often dominant influence on specimen response under cyclic loading; 2) microscale test specimens can be fabricated such that they are comprised of one dominant microstructure, thus allowing the influence of microstructure on FCGR to be evaluated quantitatively. To the best of our knowledge, no such experiment has been reported in the literature to date.

In terms of classifying mechanical testing at small length scales, the convention used in the manufacturing literature is adopted in defining the nanoscale ( $<1~\mu m$ ), the microscale ( $1-100~\mu m$ ), the mesoscale ( $100~\mu m-1000~\mu m$ ), and the macroscale (beyond  $1000~\mu m$ ) [18]. Two critical enabling factors for microscale mechanical testing are the capability of site-selective fabrication of microscale specimens via focused ion beam (FIB) machining [19] and the capability for instrumented nano/micro mechanical actuation in-situ scanning electron microscopes (SEMs) [20]. Examples of small-scale mechanical testing include uniaxial quasistatic compression and tension of nanoscale and microscale pillar specimens [21,22] and quasistatic bending of microscale cantilever beams [23,24]. In particular, using bending of pre-notched micro cantilevers for measuring fracture toughness has received attention [25].

In this paper, results are reported for FCG measurements on L-PBF AM Inconel 939 alloy (IN939) with an addition of 3 wt% Si as a minor alloying element (henceforth referred to as IN939-3Si), using microscale pre-notched cantilever specimens. IN939-3Si was chosen because its distinctive solidification microstructure makes it a good vehicle to demonstrate one major advantage of the microscale measurement protocol, namely, the ability to quantitatively assess the influence of microstructure on FCG without the influence of built-in volumetric defects. Cyclic mechanical loading is accompanied by detailed structural characterization and fractography. Also presented are discussions regarding microscale measurements and relating measured results to microstructure.

# 2. Methods

Commercial gas atomized IN939 powders (Carpenter Additive, USA) were used as the AM feedstock. IN939 powders and commercial Si particles (99.5 %+, Alfa Aesar, USA) were mixed in a SPEX 8000m MIXER for 10 h. Disk-shaped IN939-3Si specimens with dimensions of 10 mm  $\times$  10 mm  $\times$  6 mm were fabricated through LPBF-AM using a custom-built selective laser melting machine under a flowing argon atmosphere. The parameters of LPBF-AM processing were: layer thickness = 0.05 mm, laser power = 160 W, laser scan speed = 100 mm/s, and hatch space = 0.05 mm. A simple "back-and-forth" scanning strategy was adopted, with no rotation across layers. Further details on the alloy composition and the LPBF-AM process were reported previously [26]. Details on the design and construction of the custom LPBF-AM instrument have been reported elsewhere [27,28].

FCG measurements were carried out on one-end-attached microscale IN939-3Si cantilever beams. Focused ion beam machining was used to fabricate cantilevers on a Xe<sup>+</sup> plasma focused ion beam/scanning electron microscope (PFIB/SEM, ThermoFisher Helios G4) at a Xe<sup>+</sup> beam voltage of 30 kV. An as-printed IN939-3Si specimen was mechanically polished to a disk with parallel top and bottom surfaces and a right-angle edge. An array of one-end attached cantilevers is milled out by PFIB

along the edge, as illustrated in the schematic of Fig. 1(a). Fig. 1(b) shows a low magnification image of an array of tested cantilevers. Successively decreasing Xe<sup>+</sup> beam currents were used during FIB milling to generate smooth cantilever surfaces. A sharp pre-notch was cut into the top surface of the cantilever, using 30 kV Xe<sup>+</sup> beam at 4 nA in the line-milling mode. Fig. 1(c) shows a magnified view of one pre-notched square cantilever. Fig. 1(d) shows another pre-notched cantilever prior to cyclic loading in-situ an SEM. The cantilever top and front surfaces, beam width B, and beam thickness t are indicated in Fig. 1(c). The Cartesian coordinate system shown in Fig. 1(c) has X parallel to the cantilever long axis and Z normal to the cantilever front surface. The beam thickness t, pre-notch depth  $a_0$ , remaining beam thickness  $h_0$ , and load length  $l_L$  are indicated in Fig. 1(d). As shown in Fig. 1(c), typical cantilever width B, thickness t, and total length are respectively  $\sim$ 25 µm,  $\sim$ 25 µm, and  $\sim$ 100 µm. The distance between the cantilever attachment and the pre-notch ranged between 20 and 25  $\mu m$ . The depth of the prenotch  $a_0$  is ~8 µm. Bending load, as illustrated in Fig. 1(d), was applied near the cantilever end away from the pre-notch in-situ an SEM (FEI Quanta3D FEG). The loading was applied through a flat-ended Si punch. Geometric parameters of the specimen, B, t,  $a_0$ , and  $l_L$  were measured for each cantilever. All cantilevers were fabricated from as-printed IN939-

Cyclic bending of IN939-3Si cantilevers was executed using an instrumented uniaxial nanomechanical actuator (FemtoTools NMT-04). In all experiments reported here, a sinusoidal load was applied at a frequency of 100 Hz. Fig. 2 illustrates continuous stiffness measurements during cyclic bending of pre-notched cantilevers. Fig. 2(a) and (b) show respectively compression force versus time near the beginning and in the middle of one test. Fig. 2(c) and (d) show the corresponding plots of compression force versus actuator displacement for the loading cycles shown respectively in Fig. 2(a) and (b). The minimum bending load  $F_{\min}$ and maximum load  $F_{\text{max}}$  were set respectively at 4500  $\mu N$  and 49500  $\mu N$ , at a constant load ratio  $R = F_{min}/F_{max} = 1/11$ . The load force F and actuator total displacement D were recorded continuously versus time. Prior to loading on the cantilever, the actuator system stiffness was measured by compressing the flat-ended Si punch onto a solid land part of the specimen, away from the cantilever. This system compliance was subtracted from D during cantilever compression to yield the force Fversus true displacement d, from which the bending stiffness of the cantilever S = F/d was obtained, as shown in Fig. 2(c) and (d).

The length of the fatigue crack was assessed through measuring the bending stiffness of the cantilever during cyclic loading. Fig. 3(a) shows the measured stiffness *S* versus the number of load cycles *N*, for the same cantilever whose loading history was shown in part in Fig. 2. An initial slow decrease of S was observed, followed by a more precipitous drop to  $\sim$ 33 % of the initial stiffness, at which point the test was stopped. The two red arrows in Fig. 3(a) highlight the two points on the S - N curve corresponding to the two load and displacement data sets shown in Fig. 2. To relate this decrease in S to an increase in the fatigue crack length a from the initial depth of the pre-notch  $a_0$ , elastic finite element method (FEM) simulations were conducted using the FEM software package ANSYS® to calculate the bending stiffness of a cantilever with a crack. Fig. 3(b) shows one such FEM mesh used, with the cantilever width  $B = 25 \,\mu\text{m}$ , thickness  $t = 25 \,\mu\text{m}$ , and a crack length  $a = 12 \,\mu\text{m}$ . The cantilever was rigidly attached at the left end. The distance between the attachment and the crack was 20  $\mu$ m. The load length  $l_L$  was 63  $\mu$ m. A number of downward loads at the right end of the cantilever were applied and the downward displacements of cantilever end were measured, from which the bending stiffness was calculated. The 10-node 3D tetrahedral structural solid element SOLID187 was used. Convergence was demonstrated when decreasing the element size from 1  $\mu m$  to  $0.5 \mu \text{m}$  led to results differing by < 5 %. Fixing  $B = 25 \mu \text{m}$  and  $t = 25 \mu \text{m}$ , Fig. 3(c) plots the results of S versus a from a series of FEM simulations, conducted by varying the distance between the cantilever attachment to the crack in the range of 20–25  $\mu$ m,  $l_L$  in the range of 59–65  $\mu$ m, and a in the range of 0-20 µm. These ranges encompass parameters measured in

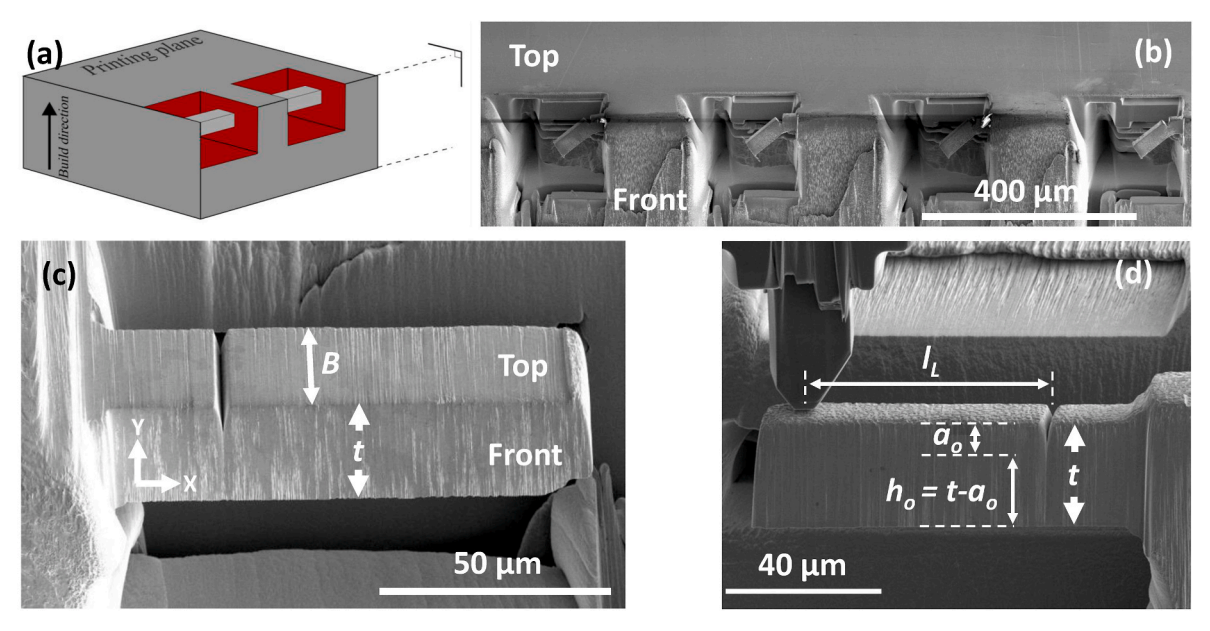


Fig. 1. PFIB fabrication of microscale IN939-3Si cantilever beams with pre-notches: (a) a schematic illustrating a milled array of one-end attached cantilevers from a disk with parallel top and bottom surfaces and a right-angle edge; (b) a low-magnification image of a tested array of cantilevers; (c) a magnified view of one typical pre-notched square cantilever; (d) another pre-notched cantilever prior to cyclic loading in-situ an SEM. The L-PBF AM build direction and printing plane are indicated in (a).

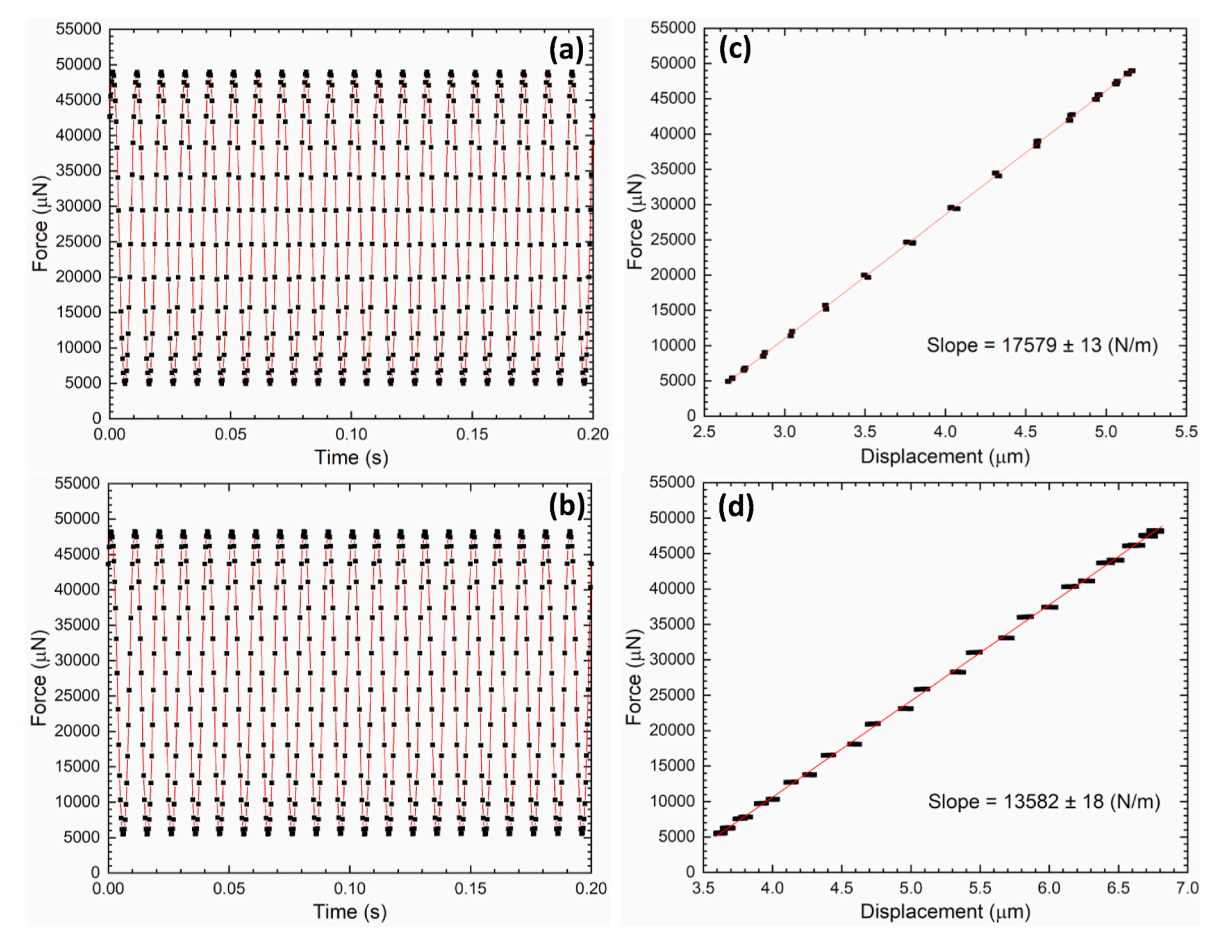
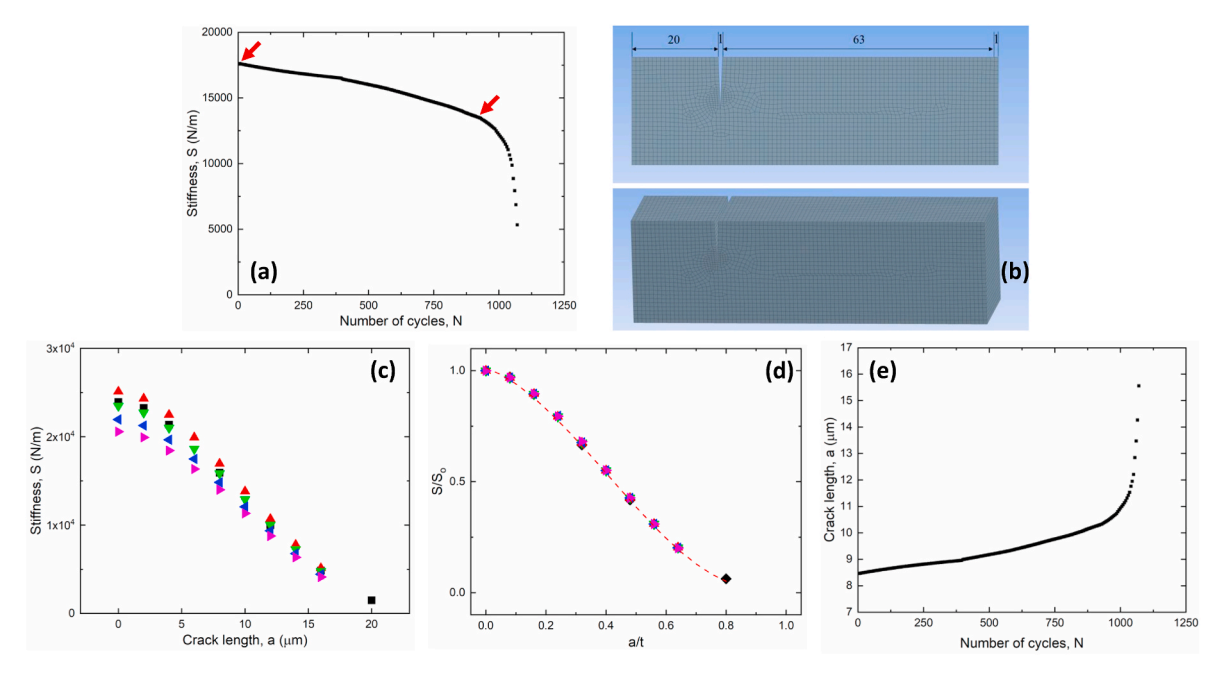


Fig. 2. Stiffness measurements during cyclic bending of pre-notched cantilevers: compression force versus time curves (a) near the beginning and (b) in the middle of one test; (c/d) compression force versus actuator displacement for the loading cycles shown respectively in (a) and (b). The red lines through the data points in (a/b) are guides to the eye. The red lines in (c/d) are least squares fits to the data. (For interpretation of the references to colour in this figure legend, the reader is referred to the Web version of this article.)



**Fig. 3.** Estimating fatigue crack length increase from measured bending stiffness decrease: (a) measured stiffness versus number of cycles; (b) one mesh used for elastic FEM simulation of bending stiffness of a cantilever with a crack; (c) calculated bending stiffness S versus crack length a for varying distances from cantilever attachment to crack and varying load spans  $l_L$ ; (d) normalized stiffness versus normalized crack length for all cases shown in (c); (e) crack length a versus number of cycles S converted from the S-N curve shown in (a).

the experiments. The calculated stiffness at a = 0 is defined as  $S_0$ . Fig. 3 (d) plots the stiffness normalized to that of the cantilever without a crack,  $S/S_0$ , versus crack length normalized to cantilever thickness, a/t. Within the range of parameter variations,  $S/S_0$  conforms to a single function of a/t to an accuracy of a few percent. The red dashed curve in Fig. 3(d) represents a cubic polynomial fit to the FEM results of  $S/S_0$ versus a/t. Within the parameter range used in the FEM simulations (and encountered in the experiments), this polynomial fit thus relates  $S/S_0$  to a/t. To convert measured S-N curves to curves of a-N, the pre-notch length  $a_0$  was measured from the final fracture surface (vide infra) and the value of  $a_0/t$  computed. The value of  $S/S_0$  at the beginning of cyclic loading is then derived from the polynomial fit to  $S/S_0$  versus a/t. Subsequent *S* values ( $S < S_o$ ) were then converted to crack length a ( $a > S_o$ )  $a_0$ ) through the  $S/S_0$  versus a/t relationship. Fig. 3(e) shows the a-Ncurve converted from the measured S - N curve shown in Fig. 3(a). All raw S - N data were converted to a - N curves following the procedure described above. Once a - N curves were obtained, da/dN versus N was calculated numerically.

Specimen characterization using SEM, X-ray energy dispersive spectroscopy (EDS), and electron backscatter diffraction (EBSD) was carried out on the Helios G4 PFIB/SEM, which housed an Oxford EDS/ EBSD system. EDS mapping and EBSD mapping were conducted at electron beam voltage and current of 20 kV and 1.6 nA, respectively. High resolution SEM imaging was conducted in the immersion mode at electron beam voltages of 2 kV and 5 kV. Details of X-ray computed tomography (XCT), X-ray diffraction (XRD), and scanning/transmission electron microscopy (S/TEM) examinations were reported previously [26] and are not repeated here. The key steps of the microscale cyclic loading experiment include mechanical polishing of as-printed specimens to define well-polished sample external surfaces perpendicular and parallel to the AM build direction, reproducible PFIB milling to fabricate cantilevers with smooth external surfaces and pre-notches, cyclic compression of cantilever with well-controlled  $F_{\min}$ ,  $F_{\max}$ , and loading frequency, and reliable conversion of raw force-displacement data to bending stiffness S.

### 3. Results and discussion

Previous XRD and TEM analysis performed on as-printed IN939-3Si specimens showed that the dominant phase within is the  $\gamma$  matrix. No  $\gamma'$  phase was observed. Additional precipitates form due to addition of the Si alloying element. EBSD examinations showed that as-printed IN939-3Si has a strong  $<\!001>$  texture, with the  $<\!001>$  direction showing a strong alignment with BD. SEM and S/TEM EDS analysis showed that the predominant precipitates are rich in Si, Ti, and Nb. These precipitates formed cells aligned with BD, with a typical cell size on the micron scale [26]. This strong directionality of the IN939-3Si solidification microstructure makes as-printed IN939-3Si a good vehicle for demonstrating the present microscale FCG measurement protocol. Previous XCT data also indicated that as-printed IN939-3Si specimens are free of volumetric pores and cracks [26].

Fig. 4 shows results of EBSD mapping of the front surface of one prenotched cantilever fabricated from as-printed IN939-3Si. The IN939-3Si specimen was oriented such that the cantilever long axis (Fig. 4(a), Xdirection) was perpendicular to BD. This cantilever orientation is thus dubbed "transverse". For transversely oriented cantilevers, the PFIB milled pre-notch is parallel to BD (Y-direction). The EBSD mapping area covered most of the cantilever thickness. The EBSD band contrast image shown in the inset of Fig. 4(a) shows a clear columnar structure, with the columns largely aligned with BD. Consistent with the band contrast image, the inverse pole figure (IPF) maps, Fig. 4(b), (c), and (d), all show the same columnar structure. The IPF-Y map shown in Fig. 4(c) shows a dominant <001> orientation, consistent with a strong <001> texture aligned with BD. The results of EDS mapping of the front surface of the same cantilever are shown in Fig. 5. Comparing Figs. 4 and 5, it is evident that the columnar structure apparent in Fig. 4 is accentuated by the cell structure of the precipitates, rich in Si, Ti, and Nb. The Ni, Co, and Cr compositions within the  $\gamma$  matrix appear to be uniform. Fig. 6 shows the results of EDS mapping of the top surface of the same cantilever. The cell structure of the precipitates, rich in Si, Ti, and Nb, is evident, with a typical cell size of 2–3 µm.

Fig. 7 shows results of EBSD mapping of the front surface of another pre-notched IN939-3Si cantilever fabricated out of the same as-printed

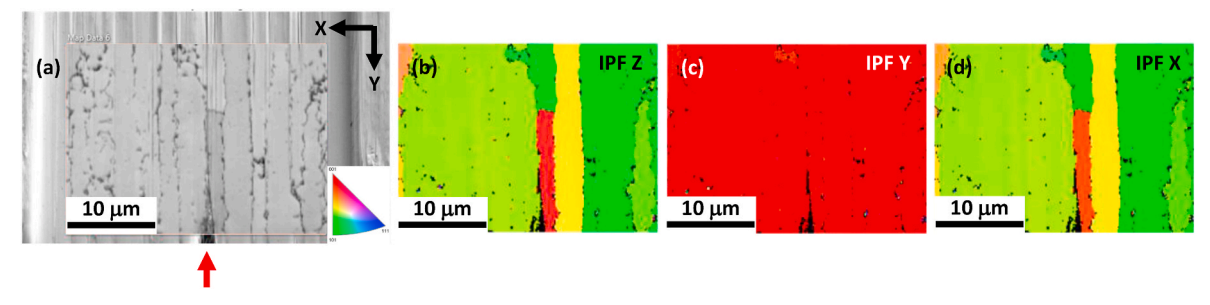
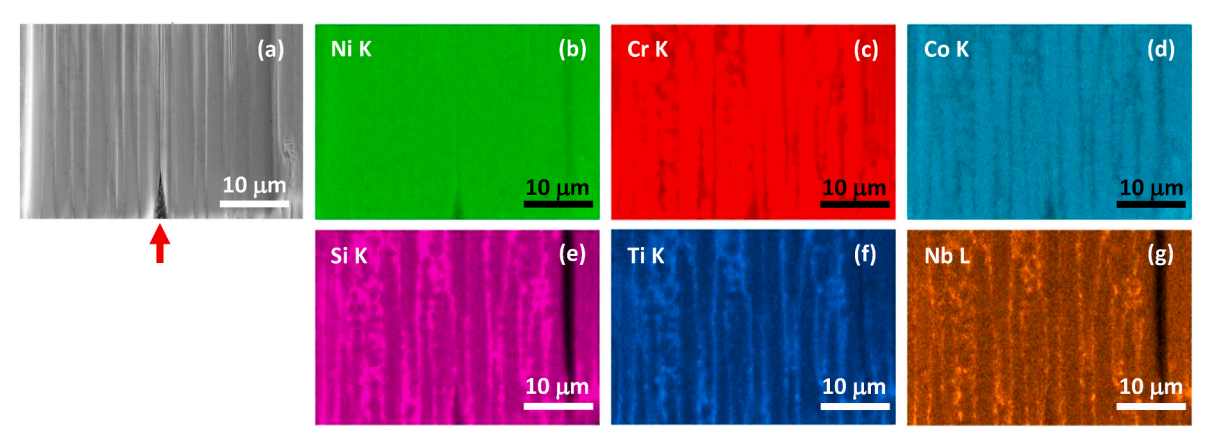


Fig. 4. EBSD mapping of one pre-notched IN939-3Si cantilever in the transverse orientation: (a) an SEM image of the cantilever front surface including the PFIB milled pre-notch (highlighted by the red arrow); (b/c/d) inverse pole figure (IPF) Z, Y, X maps. The inset in (a) is the band contrast image of the EBSD mapping area. (For interpretation of the references to colour in this figure legend, the reader is referred to the Web version of this article.)



**Fig. 5.** EDS mapping of the front surface of the same pre-notched IN939-3Si cantilever shown in Fig. 4: (a) an SEM image of the cantilever front surface including the PFIB milled pre-notch (highlighted by the red arrow); (b/c/d) corresponding X-ray intensity maps of Ni K, Cr K, and Co K; (e/f/g) corresponding X-ray intensity maps of Si K, Ti K, and Nb L. (For interpretation of the references to colour in this figure legend, the reader is referred to the Web version of this article.)

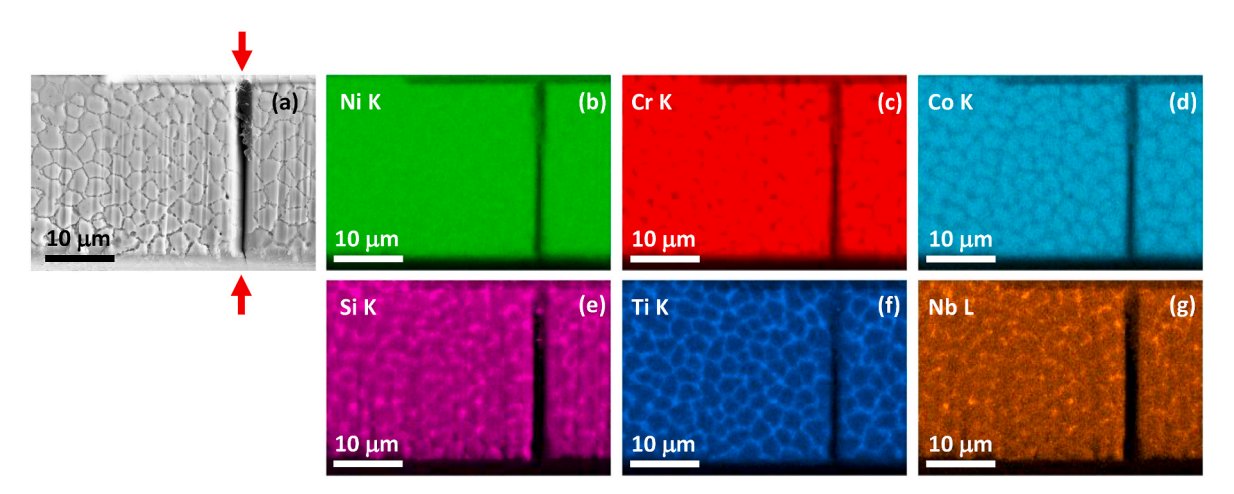
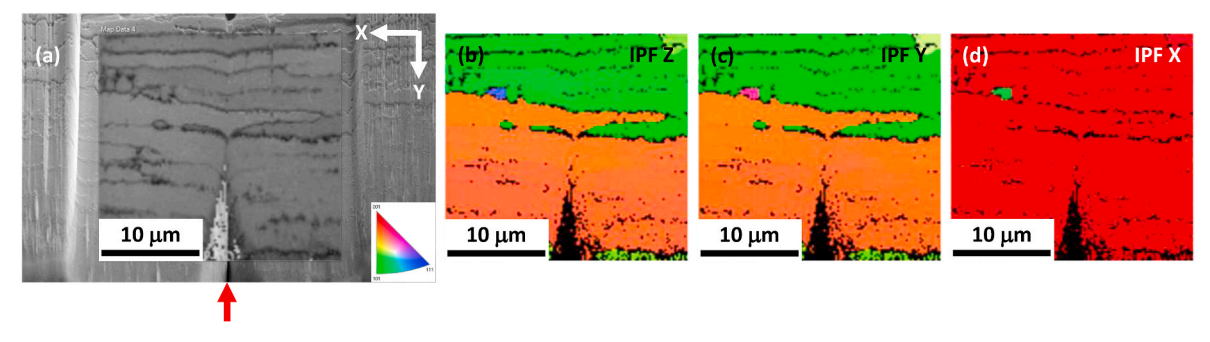


Fig. 6. EDS mapping of the same pre-notched IN939-3Si cantilever shown in Fig. 4: (a) an SEM image of the cantilever top surface including the PFIB milled pre-notch (highlighted by the red arrows); (b/c/d) corresponding X-ray intensity maps of Ni K, Cr K, and Co K; (e/f/g) corresponding X-ray intensity maps of Si K, Ti K, and Nb L. (For interpretation of the references to colour in this figure legend, the reader is referred to the Web version of this article.)

IN939-3Si. Here, the IN939-3Si specimen was rotated 90° such that the cantilever long axis (Fig. 7(a), X-direction) was parallel to BD. This cantilever orientation is thus dubbed "longitudinal". For longitudinally oriented cantilevers, the PFIB milled pre-notch is now perpendicular to BD (X-direction). The EBSD band contrast image shown in the inset of Fig. 7(a) shows the same columnar structure aligned with BD. The EBSD mapping area again covered most of the cantilever thickness. Consistent with the band contrast image, the inverse pole figure (IPF) maps, Fig. 7 (b), (c), and (d), all show the same columnar structure. The IPF-X map

shown in Fig. 7(d) again shows a dominant <001> orientation, consistent with the data shown in Fig. 4. The results of EDS mapping of the front surface of the same cantilever are shown in Fig. 8, again showing the same columnar structure accentuated by the cell structure of the Si, Ti, and Nb rich precipitates. EDS mapping of the top surface of the same cantilever is shown in Fig. 9, which shows similar alignment of Si, Ti, and Nb rich precipitates along the cantilever long axis, and uniform Ni, Co, and Cr compositions within the  $\gamma$  matrix. Data shown in Figs. 7–9 exhibit the same columnar structure documented in Figs. 4–6.



**Fig. 7.** EBSD mapping of one pre-notched IN939-3Si cantilever in the longitudinal orientation: (a) an SEM image of the cantilever front surface including the PFIB milled pre-notch (highlighted by the red arrow); (b/c/d) inverse pole figure (IPF) Z, Y, X maps, respectively. The inset in (a) is the band contrast image of the EBSD mapping area. (For interpretation of the references to colour in this figure legend, the reader is referred to the Web version of this article.)

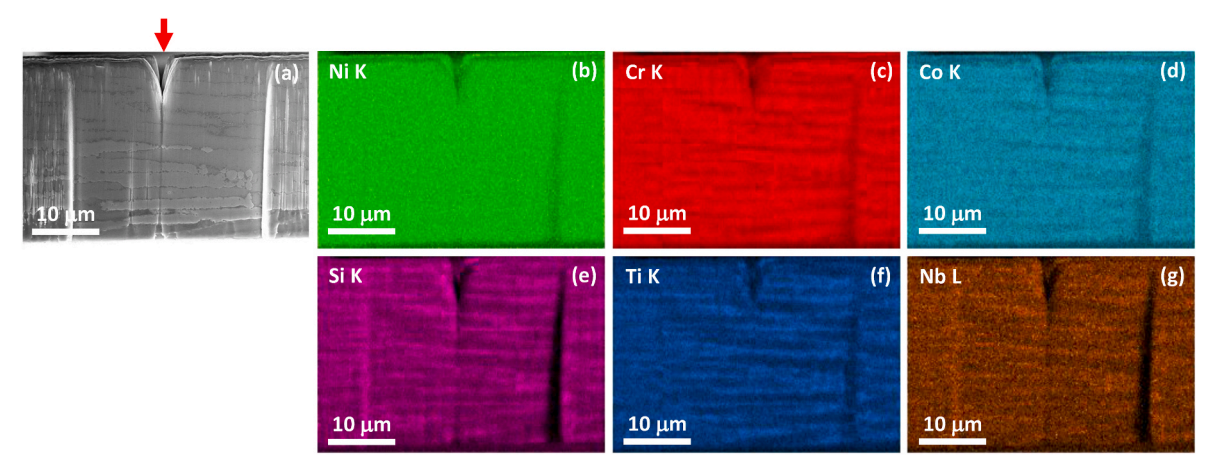
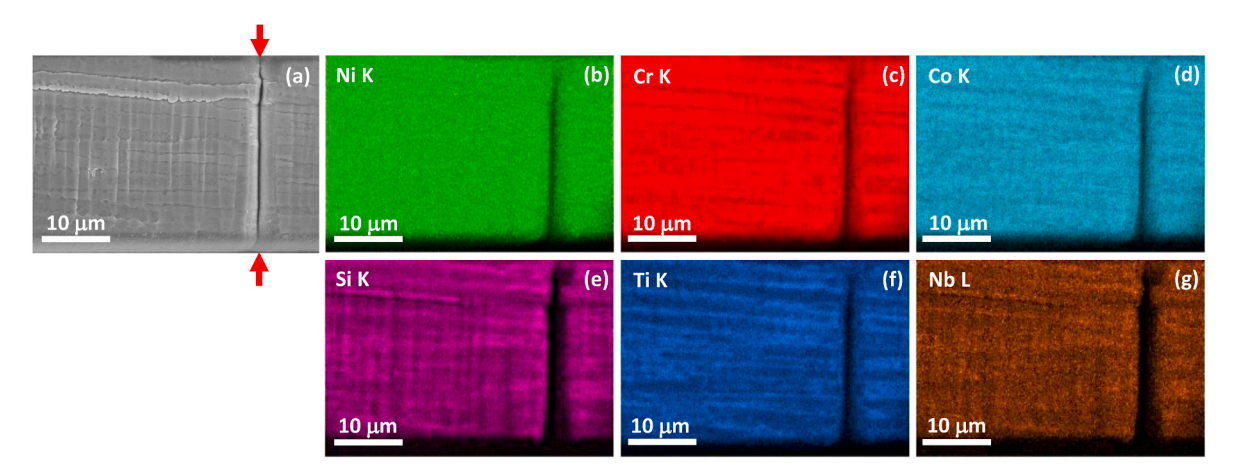


Fig. 8. EDS mapping of the same pre-notched IN939-3Si cantilever shown in Fig. 7: (a) an SEM image of the cantilever front surface including the PFIB milled pre-notch (highlighted by the red arrow); (b/c/d) corresponding X-ray intensity maps of Ni K, Cr K, and Co K; (e/f/g) corresponding X-ray intensity maps of Si K, Ti K, and Nb L. (For interpretation of the references to colour in this figure legend, the reader is referred to the Web version of this article.)



**Fig. 9.** EDS mapping of the same pre-notched N939-3Si cantilever shown in Fig. 7: (a) an SEM image of the cantilever top surface including the PFIB milled pre-notch (highlighted by the red arrows); (b/c/d) corresponding X-ray intensity maps of Ni K, Cr K, and Co K; (e/f/g) corresponding X-ray intensity maps of Si K, Ti K, and Nb L. (For interpretation of the references to colour in this figure legend, the reader is referred to the Web version of this article.)

By orienting the IN939-3Si specimen differently, the pre-notch can be placed either parallel or perpendicular to BD, and by extension, at any inclination with respect to BD.

After the programmed cyclic loading completed, the actuator was used to exert a final, quasi-static push downward to bend the cracked cantilever as far as possible, so that the fracture surface is revealed to the maximum extent. Fig. 10 shows results of cyclic loading of one IN939-

3Si cantilever in the transverse orientation, which serves to demonstrate the correspondence between fatigue crack length deduced from cantilever bending stiffness measurements and examination of the actual fracture surface. Fig. 10(a) shows the a-N curve obtained from stiffness measurements on one transversely oriented IN939-3Si cantilever, the same curve as that shown in Fig. 3(e). Fig. 10(b) shows an SEM image of the corresponding fracture surface, showing the PFIB machined

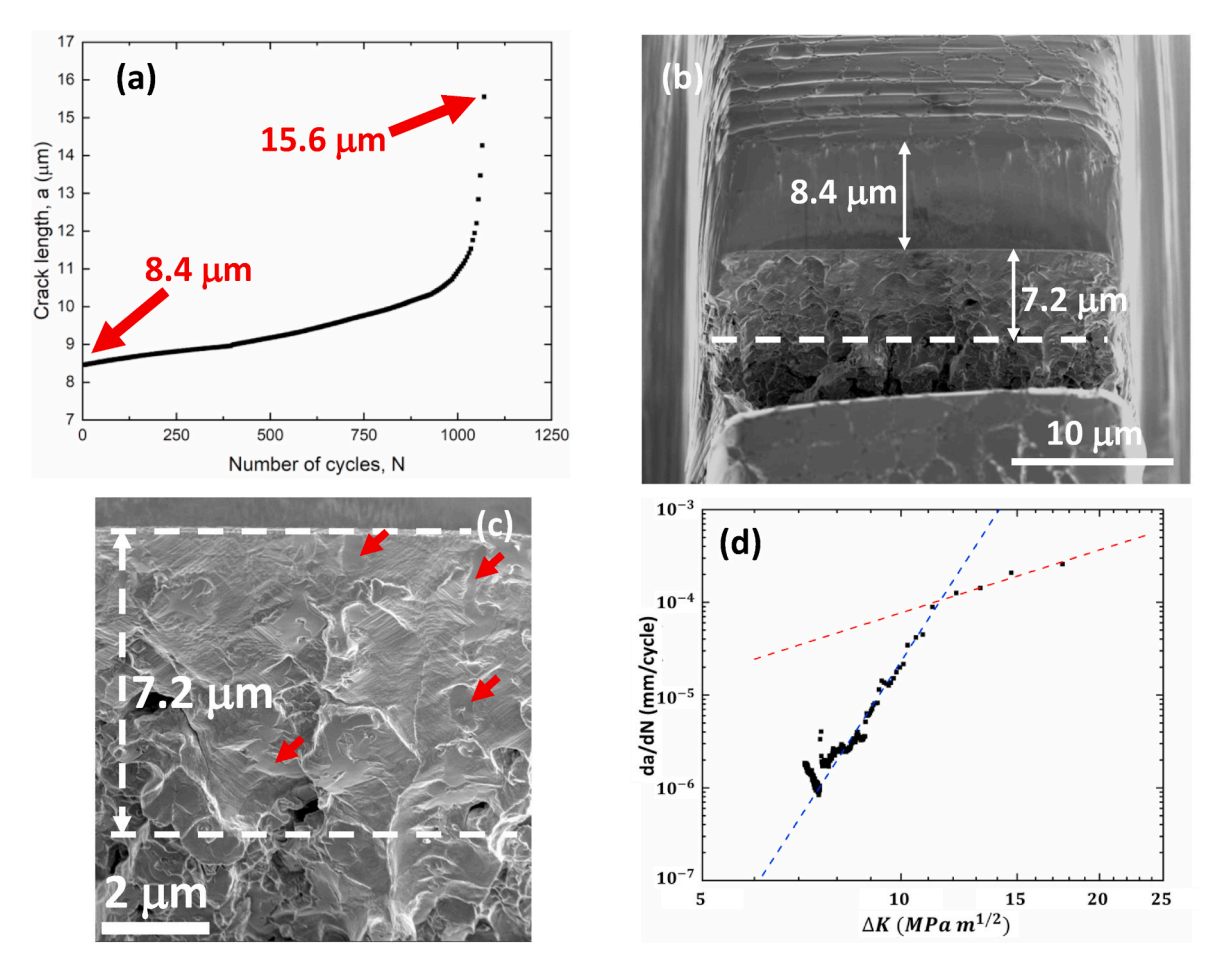


**Fig. 10.** Cyclic loading of one IN939-3Si cantilever in the transverse orientation: (a) crack length *a* vs. number of loading cycles *N*; (b) an SEM image of the fracture surface showing the PFIB machined pre-notch, the approximate location of the end of FCG zone, and the additional fracture caused by further quasi-static compression of the cyclically loaded beam; (c) a higher magnification image of a portion of the same fracture surface; (d) the deduced fatigue crack growth curve.

pre-notch, the approximate location of the end of FCG zone, and the additional fracture caused by further quasi-static compression of the cyclically loaded beam. The length of the PFIB milled pre-notch  $a_0$ , ~8.4 μm in this case, is easily identified by its smooth surface. As discussed in the methods section, this measurement of  $a_0$  determines the initial point of the a - N curve shown in Fig. 10(a) (and Fig. 3(e)), according to which the final length of the fatigue crack should be 15.6 µm, as indicated by the white dashed line in Fig. 10(b). The higher magnification image of the fracture surface shown in Fig. 10(c) shows the Si, Ti, and Nb rich precipitates (as highlighted by the red arrows), as well as fine striations commonly observed on fatigue fracture surfaces of alloys with a reasonable toughness [29]. These fatigue striations appeared in the fatigue crack growth zone and did not appear on the additional fracture surface caused by the final quasi-static push of the actuator. An approximate location of the end of the FCG zone was thus identified by the presence or absence of fatigue striations. The two dashed white lines in Fig. 10(c) highlight, respectively, the locations corresponding to the end of the PFIB milled pre-notch and the demarcation between the presence and absence of fatigue striations, the distance between which is  $\sim$ 7.2 µm. Thus, the comparison between Fig. 10(a) and (c) shows a good correspondence between the final fatigue crack length estimated from the stiffness-based method and that based on observations made on the actual fracture surface. This correspondence confirms that the present procedure used to infer the length of the fatigue crack from measured bending stiffness is sound. Once the correctness of the a-N curve shown in Fig. 10(a) was confirmed, a previously reported FEM simulation for the mode I stress intensity factor  $K_I$  for a cracked cantilever was used to calculate  $K_I$  as a function of the bending load F and the crack length a

[30]

$$K_{I} = \frac{Fl_{L}}{Bt^{3/2}}f(a/t),$$
 (1)

and

$$f(a/t) = 77.608(a/t)^3 - 48.422(a/t)^2 + 24.184(a/t)^1 + 1.52.$$
 (2)

As noted, the geometry parameters  $l_L$ , B, t, were measured for each cantilever experiment. Fig. 10(d) plots the FCG curve, i.e., crack growth rate da/dN versus stress intensity factor range  $\Delta K$ , where  $\Delta K = K_I(F_{max}) - K_I(F_{min}) = (1-R)K_{max}$  and  $K_{max} = K_I(F_{max})$ . Data shown in Fig. 10(d) exhibit both the threshold regime and the Paris-law crack growth regime [27]. The blue and red dashed lines in Fig. 10(d) are power law fits to the threshold and Paris-law regimes of the fatigue crack growth data, with a clear transition between them.

Fig. 11 summarizes the present FCGR data. Fig. 11(a) and (b) show, respectively, the da/dN -  $\Delta K$  curve obtained from one cantilever in the transverse orientation and one in the longitudinal orientation. Again, data shown in Fig. 11(a) and (b) exhibit both the threshold regime and the Paris-law regime. Two separate power law fits, shown respectively by the blue and red dashed lines in Fig. 11(a) and (b), describe the data in the threshold regime and the Paris law regime reasonably well. The intersection between the two power law fits with distinctly different exponents marks the transition between the two regimes. The power law fit to the data in the Paris law regime,  $da/dN = C(\Delta K)^m$ , yields the Paris law exponent m. The threshold stress intensity factor  $\Delta K_{th}$  was taken to be the  $\Delta K$  value at which the threshold regime power law fit extrapolates to  $da/dN = 10^{-7}$  mm/cycle, or 1 Å/cycle. Fig. 11(c) and (d) show,

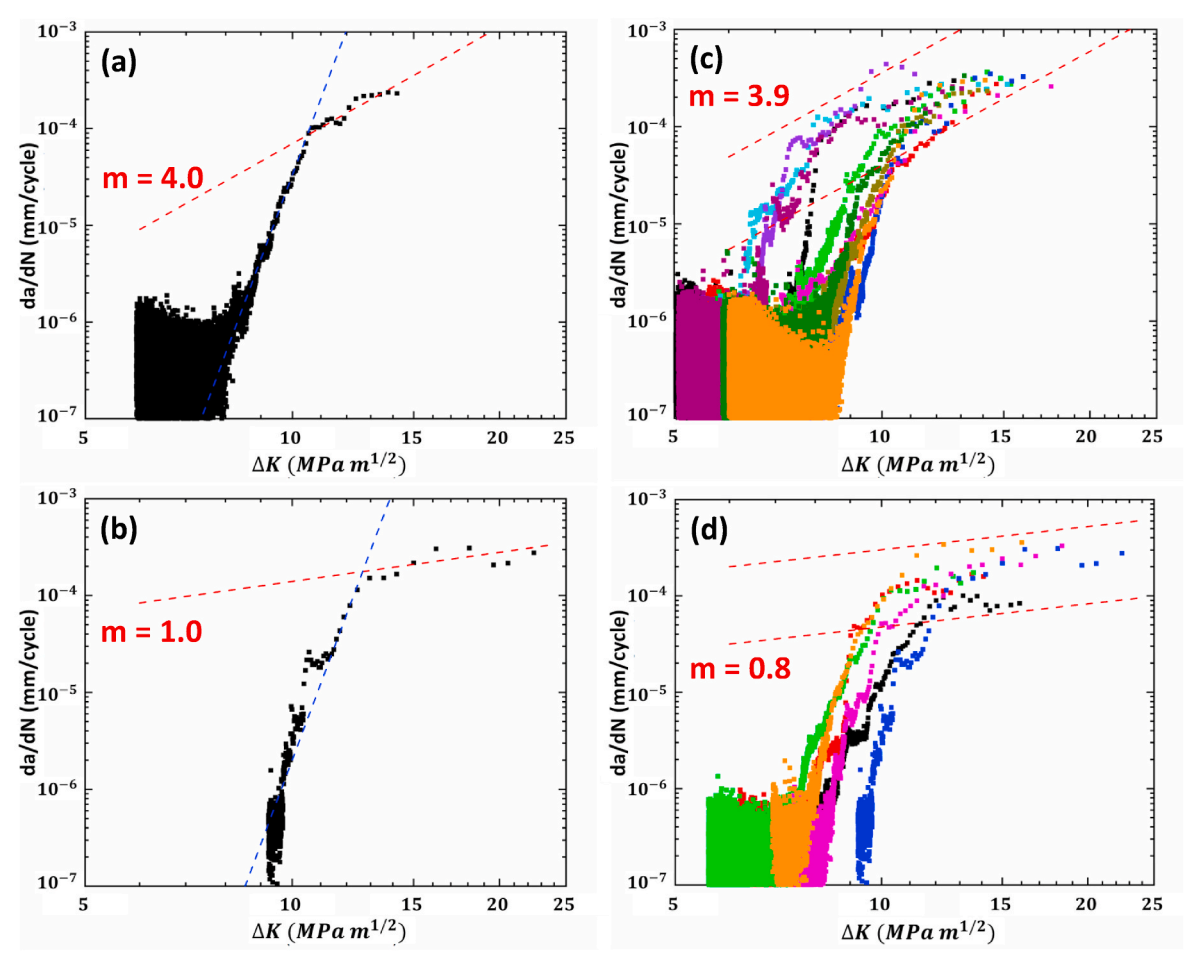


Fig. 11. FCGR measured from IN939-3Si cantilevers: a da/dN -  $\Delta K$  curve measured from (a) one cantilever in the transverse and (b) one cantilever in the longitudinal orientation; a collection of da/dN -  $\Delta K$  curves measured from (c) 11 cantilevers in the transverse orientation and (d) 6 cantilevers in the longitudinal orientation.

respectively, a collection of  $\mathrm{d}a/\mathrm{d}N$  -  $\Delta K$  curves measured from 11 cantilevers in the transverse orientation and one measured from 6 cantilevers in the longitudinal orientation. Two separate power law fits were conducted respectively on data in the threshold regime and the Paris law regime for each cantilever. Tables 1 and 2 summarize, respectively, results of testing the group of 11 transversely oriented cantilevers and the other group of 6 longitudinally oriented ones. First, it is noted that the values of  $\Delta K_{th}$  were essentially the same for transversely and longitudinally oriented cantilevers, the former being  $6.8 \pm 1.1 \ MPa \ m^{1/2}$  and the latter  $7.2 \pm 0.9 \ MPa \ m^{1/2}$ . Second, all  $\mathrm{d}a/\mathrm{d}N$  -  $\Delta K$  curves shown in

**Table 1** Results of power law fits to fatigue crack growth data obtained from 11 transversely oriented cantilevers. The Paris law exponent m averaged over the 11 independent measurements is 3.9  $\pm$  2.1. The averaged threshold stress intensity factor  $\Delta K_{th}$  is 6.8  $\pm$  1.1  $MPa\,m^{1/2}$ .

Cantilever #	Paris-law exponent, m	Threshold stress intensity factor, $\Delta K_{th}$ (MPa $m^{1/2}$ )
1	2.3	7.2
2	6.0	7.7
3	5.0	6.9
4	5.0	8.3
5	1.5	4.7
6	2.3	6.1
7	6.5	6.2
8	4.0	7.3
9	2.3	5.2
10	7.0	7.9
11	1.5	7.5

**Table 2** Results of power law fits to fatigue crack growth data obtained from 6 longitudinally oriented cantilevers. The Paris law exponent m averaged over the 6 independent measurements is  $0.8 \pm 0.6$ . The averaged threshold stress intensity factor  $\Delta K_{th}$  is  $7.2 \pm 0.9~MPa~m^{1/2}$ .

Cantilever #	Paris-law exponent, m	Threshold stress intensity factor, $\Delta K_{th}$ (MPa $m^{1/2}$ )
1	0.0	7.0
2	1.0	7.4
3	1.3	6.6
4	0.2	5.8
5	1.0	7.5
6	1.5	8.6

Fig. 11 exhibit both the threshold regime and the Paris-law crack growth regime. Third, the scatter of the Paris law exponent m within the transverse orientation test group is larger than that within the longitudinal orientation test group, 1.5–7.0 in the former case and 0.0–1.5 in the latter. Despite the scatter, the present measurements reveal a significant difference in the m value for the transversely and longitudinally oriented cantilevers. The slopes of the two red dashed lines in Fig. 11(c) and (d) represent the Paris-law exponent averaged overall all measurements in the group: m averages to  $3.9 \pm 2.1$  for transversely oriented cantilevers and to  $0.8 \pm 0.6$  for longitudinally oriented ones. The averaged Paris law exponent presently measured for transversely oriented cantilevers, m=3.9, is in line with a previous study of FCG in high temperature alloys, which showed  $m \sim 3.5$  for bulk IN939 [31]. The present collection of data demonstrates, for the first time to the best of

our knowledge, that cyclic bending of pre-notched microscale cantilevers can sense both the threshold regime and the Paris-law regime of fatigue crack growth, despite the small characteristic specimen size of  $\sim\!25~\mu m$ . Furthermore, such measurements can sense a significant difference in crack growth when the direction of crack propagation is oriented differently within a given microstructure, in this case, the direction of crack propagation with respect to the pronounced columnar microstructure (BD).

Gruber et al. summarized results of FCGR measurements on L-PBF Inconel 718 (IN718) alloys conducted in several independent studies [32]: at a constant load ratio of R = 0.1, measured values of  $\Delta K_{th}$  and da/dN at the transition from the threshold regime to the Paris law regime both showed rather large variations: from  $\sim$ 3 to  $\sim$ 15 MPa m<sup>1/2</sup> for  $\Delta K_{th}$  and from  $\sim 10^{-6}$  to  $\sim 5 \times 10^{-5}$  mm/cycle for da/dN. The apparent sharpness of the threshold to Paris law regime transition also varied from study to study [30]. The presently measured values of  $\Delta K_{th}$ ,  $\sim$ 7 MPa  $m^{1/2}$  are in line with those obtained from macroscopic FCGR measurements on L-PBF IN718 alloys. A similar statement can be made about the presently measured da/dN values at the threshold to Paris law regime transition, which ranges from  $4 \times 10^{-5}$  to  $\sim 1 \times 10^{-4}$  mm/cycle. It is noted that a much more uniform microstructure is contained within the present microscale cantilever specimens as compared to conventional macroscale FCG specimens, while the physical dimensions of the present micro cantilevers are much smaller than the macroscale specimens. Whether the rather sharp transition from the threshold regime to the Paris law regime exhibited in the present measurements is due to the increased microstructural uniformity or the small specimen size needs to be ascertained through additional studies.

Fig. 12 shows typical fatigue fracture surface morphologies of cyclically loaded microscale IN939-3Si cantilevers. Fig. 12(a) and (b) show respectively fracture surfaces of one transversely and one longitudinally oriented cantilever. Fig. 12(a) exhibits a morphology typical of

transgranular fatigue fracture surfaces, decorated by exposed smooth fracture surfaces of the Si, Ti, and Nb rich precipitates, indicating that these precipitates are brittle. Fig. 12(b) shows a similar transgranular fatigue fracture morphology, but in patches. Fig. 12(c) and (d) show respectively higher magnifications images of the same fracture surfaces shown in Fig. 12(a) and (b). The white arrows in Fig. 12(c) and (d) highlight fatigue striations in the  $\gamma$  matrix. The red arrows in Fig. 12(c) and (d) highlight smooth fracture surfaces of the Si, Ti, and Nb rich precipitates. The yellow line in Fig. 12(c) and green line in Fig. 12(d) mark, respectively, distances spanned by 10 and 20 fatigue striations, which are respectively ~180 nm and ~340 nm in length. In Fig. 12(c), the precipitates, easily distinguishable by their smooth fracture surfaces, are seen to line up approximately along the direction of crack propagation, or BD. In Fig. 12(d), the transgranular fracture surface patch of the y matrix is seen to be surrounded by an approximately circular arrangement of precipitates. Such observations are consistent with the precipitate cell structure documented in Figs. 4–9. In particular, fracture surfaces of longitudinally oriented cantilevers are expected to exhibit Si, Ti, and Nb rich precipitates in approximately circular cells (e.g., compare Figs. 12(d) and 6). In both Fig. 12(c) and (d), the fatigue striations observed in the  $\gamma$  matrix demonstrate that cyclic bending of the microscale cantilevers has indeed led to fatigue crack propagation through the crack blunting mechanism [27]. The average spacing between successive fatigue striations in the  $\gamma$  matrix, highlighted by the yellow line and green line shown respectively in Fig. 12(c) and (d), appears to be similar in magnitude regardless of the cantilever orientation: ~18 nm in Fig. 12(c) and ~17 nm in Fig. 12(d). Thus, the significant difference in fatigue crack growth when the crack propagates parallel or perpendicular to the build direction in the present IN939-3Si cantilevers, as manifested by the significantly different m values, apparently results from the difference in microstructure, specifically, the arrangement of the cell structure of the brittle precipitates with respect

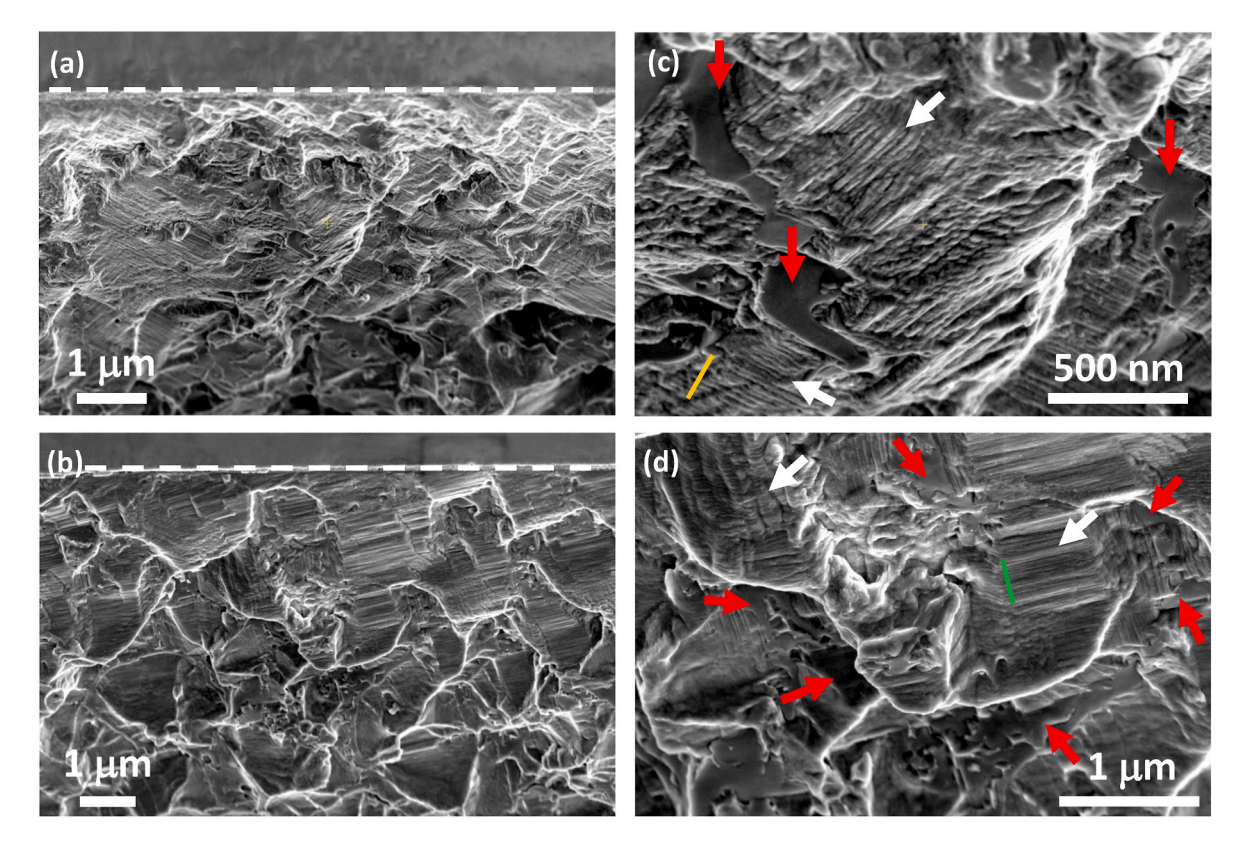


Fig. 12. Fracture surface morphology of cyclic loaded IN939-3Si cantilevers: a lower magnification SEM image of the fracture surface of (a) one cantilever in the transverse orientation and (b) one cantilever in the longitudinal orientation; (c/d) a higher magnification image of the same fracture surface shown in (a) and (b). The white dashed lines in (a) and (b) highlight the ends of PFIB milled pre-notches.

to the direction of crack propagation. It is noted that a lower value of the Paris law exponent m means that the dependence of  $\mathrm{d}a/\mathrm{d}N$  on  $\Delta K$  is less pronounced (in the limit of m=0,  $\mathrm{d}a/\mathrm{d}N$  is independent of  $\Delta K$ ). For a given specimen size, fatigue crack growth under loading with constant  $F_{\mathrm{max}}$  and R is slower for a lower value of m. That is, for as-printed IN939-3Si, the present measurements show that the rate of fatigue crack growth when the direction of crack propagation is perpendicular to the direction of columnar growth (BD) is significantly lower than that when crack propagation is parallel to the direction of columnar growth.

While earlier reports showed no clear consensus on the effects of microstructure-induced anisotropy on fatigue behavior from macroscale measurements [10,15,16], a more recent FCG study of L-PBF IN718 by Ghorbanpour et al. using macroscale measurements showed lower FCGR when the crack propagation direction is perpendicular to BD [33], qualitatively similar to the present data. They argued that the lower FCGR is due to the larger number of grain boundaries perpendicular to the path of the propagating crack [33]. A similar argument can be made in the present case. Because of the distinct microstructural anisotropy present within as-printed IN939-3Si, a fatigue crack propagating along BD or perpendicular to BD would see a rather different local environment. In the latter case, the propagating crack would encounter significantly more brittle precipitates, periodically interspersed and perpendicular to its path (compare e.g., data shown in Figs. 4-6 vs. those in Figs. 7-9). Each encounter serves to "reset" the speed of crack propagation and thus lower the average Paris law exponent m. It is noted that such an argument is at best heuristic, and a more detailed computational modeling/simulation effort should accompany the experimentation to achieve a better understanding, a task remaining for the future.

A comment should be made on the appropriateness of the stress intensity factor calculation, as expressed in Eqs. (1) and (2). First, it is noted that, for a cracked plate, the compliance or the inverse of the stiffness, C = 1/S, is relatable to the energy release rate G through [27].

$$G = \frac{F^2}{2B} \frac{dC}{da}.$$
 (3)

Second, it is noted that G is related to K through the G-K equivalence,

$$G = \frac{1 - \nu^2}{E} K_I^2,$$
 (4)

$$G = \frac{1}{r}K_I^2,\tag{5}$$

for plane strain and plane stress, respectively [27]. In Eqs. (4) and (5), E and  $\nu$  are respectively the Young's modulus and the Poisson's ratio. Third, it is noted that, for the present experiments,  $F_{\text{max}}$ , B, E, and  $\nu$  are constants, therefore  $\mathrm{d}C/\mathrm{d}a$  and  $K_I^2$  should have the same functional dependence with respect to the crack length a. In the present experiments, since S is measured continuously as a function of load cycle N,

and a as a function of N is derived through the FEM simulations, C is therefore known as a function of a and dC/da can be obtained numerically. The relationship between dC/da and  $K_I^2$  can thus be tested. Fig. 13 (a) shows a dC/da - a plot for one tested cantilever, on which  $K_I^2(a)$  as calculated from Eqs. (1) and (2) is superimposed. The general agreement between dC/da and  $K_I^2$  is evident. This agreement further confirms the soundness of the present measurements, as well as the previously calculated  $K_I$  as expressed in Eqs. (1) and (2) [28].

One basic issue deserving further discussion is the extent of the plastic zone ahead of the fatigue crack tip. For monotonic loading in mode I at the macroscopic scale, the size of the plastic zone ahead of the crack tip,  $r_p$ , can be related to the stress intensity factor  $K_I$  and the yield stress  $\sigma_V$  of the material:

$$r_p = \frac{1}{3\pi} \left( \frac{K_I}{\sigma_y} \right)^2, \tag{6}$$

$$r_p = \frac{1}{\pi} \left( \frac{K_I}{\sigma_v} \right)^2, \tag{7}$$

for plane strain and plane stress, respectively [27]. Micro-tensile testing of the presently-used, as-printed IN939-3Si has been conducted previously, and a yield stress value of  $\sigma_y \sim 1$  GPa was obtained from measured tensile stress – strain curves [26]. An appropriate value for  $K_I$  for the present cyclic loading situation can be chosen by examining data shown in Fig. 11. For this discussion, the  $K_I$  value was chosen to be  $\sim 12$  MPa  $m^{1/2}$ , a value within the Paris-law crack growth regime for all cantilevers whose data are shown in Fig. 11. Taking these values, an estimate of  $r_p$  would be  $\sim 15$  µm for plane strain and  $\sim 45$  µm for plane stress according to Eqs. (6) and (7). These values overestimate the actual size of the plastic zone ahead of the fatigue crack tip in the present cantilevers, as the size of the entire specimen is  $\sim 25$  µm.

Additional factors may be at play for why  $r_p$  was overestimated in the previous paragraph. In the context of measuring fracture toughness using microscale specimens, it was noted that  $\sigma_y$  values estimated from nanoindentation measurements may be more appropriate as they offer a better representation of the characteristic material flow stress when significant strain gradients are expected to be present near the crack tip [28]. Nanoindentation measurements have also been performed previously on the presently-used, as-printed IN939-3Si, and its hardness was measured to be  $\sim$ 6 GPa at small indentation depths [26]. Based on the well-known hardness-to-flow stress scaling [34], an estimate for the flow stress in the presence of significant strain gradients should be  $\sim$ 2 GPa. Taking  $K_I$  and  $\sigma_y$  respectively to be  $\sim$ 12  $MPa~m^{1/2}$  and  $\sim$ 2 GPa,  $r_p$  would be  $\sim$ 3.8  $\mu$ m for plane strain and  $\sim$ 11.4  $\mu$ m for plane stress according to Eqs. (6) and (7).

Fig. 13(b) shows an SEM image of the front surface of one transversely oriented cantilever after cyclic loading. The pre-notch depth  $a_0$  is  $\sim 8$  µm, and the fatigue crack has propagated away from the end of the

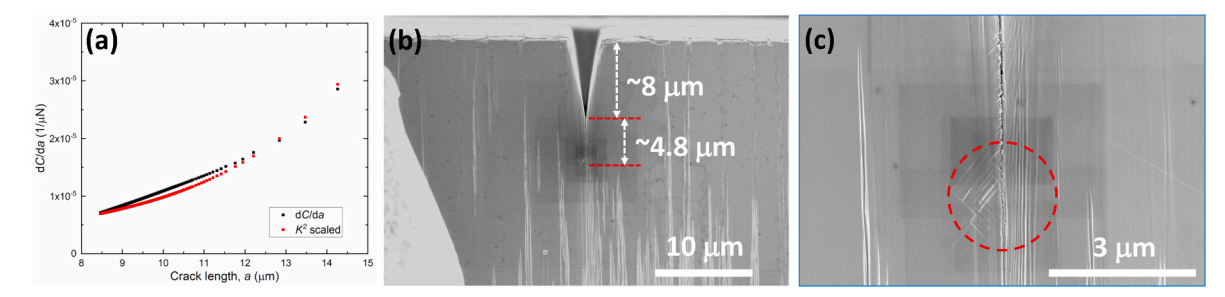


Fig. 13. (a) Measured dC/da versus a for one cracked cantilever. The curve of  $K^2$  vs. a calculated from Eqs. (1) and (2) is superimposed on the plot, scaled such that the numerical values of dC/da and  $K^2$  agree at the lowest a value. (b) a low magnification SEM image of the front surface of one transversely oriented cantilever; (c) a higher magnification image of the front surface near the tip of the same fatigue crack. The red dashed lines in (b) highlight respectively the end of the pre-notch and the location of the crack tip. The red dashed circle in (c) highlights the extent of the slip steps near the crack tip. (For interpretation of the references to colour in this figure legend, the reader is referred to the Web version of this article.)

pre-notch for  $\sim$ 4.8 µm. Fig. 13(c) shows a higher magnification image of the cantilever front surface near the crack tip. It is evident that a dense collection of slip traces appeared near the crack tip, indicating dislocation activities reaching the surface. This dense collection of slip traces is approximately enclosed within a circle with diameter of  $\sim$ 2.2  $\mu$ m, which yields an estimate, albeit a rough one, of the extent of the plastic zone near the crack tip. This value of  $\sim$ 2.2  $\mu$ m, based on the surface slip trace observations, is close to the  $r_D$  estimate in the preceding paragraph. It is noted that a previous discrete dislocation (DD) plasticity modeling of short cracks in single crystals modeled the fracture behavior as an interplay between the cohesive and plastic flow properties. Defining the plastic zone size as the spatial extent from the crack tip possessing a certain amount of slip activity or dislocation density, the DD simulations generated a plastic zone size in the micron scale [35]. A more detailed understanding of the plastic zone near the tip of a fatigue crack in microscale specimens, such as the cantilevers used in the present work, requires additional experimental characterization as well as modeling and simulation efforts, and remains a task for the future.

The fact that the present microscale test protocol for FCG measurements can sense quantitative differences in crack growth behavior when crack propagates along different directions with respect to a given microstructure opens possibilities for further AM material/process design. It has been professed that one promise offered by AM is the ability to do location-specific tailoring of the microstructure within an AM component according to the expected stress distribution within the component when it is put into service [12]. The present results show that such location-specific microstructure designs can now be assessed quantitatively through microscale tests demonstrated here. Realization of such a promise also remains a task for the future. Work is ongoing with an aim to apply such test protocol to a broader range of AM materials and processing conditions, validate experimental findings with computational models, and explore microstructure-tailored designs in application settings.

# 4. Summary

Measurements of fatigue crack growth in an as-printed L-PBF IN939-3Si alloy were conducted through cyclic bending of pre-notched cantilevers with a characteristic cross-sectional dimension of 25  $\mu m \times 25~\mu m.$ Despite the small specimen size, the cyclic bending measurements can sense both the threshold regime and the Paris-law regime of fatigue crack growth quantitatively. Fabrication of microscale cantilevers allows crack propagation to be arranged along specific directions with respect to a given microstructure. In the present experiments, FCG measurements were conducted with the direction of crack propagation in parallel with or perpendicular to the L-PBF build direction, with no influence from built-in volumetric defects. Significant differences in FCG behavior were observed when the direction of fatigue crack propagation is parallel or perpendicular to the columnar microstructure of as-printed IN939-3Si: crack growth rate is slower when the propagation direction is perpendicular, as evidenced by the substantially smaller value of the Paris law exponent. The present work demonstrates the efficacy of measuring FCG using microscale specimens, which offers the advantage of being able to quantitatively sense the influence of a given microstructure on crack growth as well as facilitating the understanding of the associated crack propagation mechanisms. The present study focused on one specific alloy system with a particular microstructure. The applicability and limitation of the presently described microscale test protocol need to be clarified through generalization to other AM materials in the future. The influence of the pre-notch geometry and loading frequency also needs to be better understood through future experimentation.

# Data statement

Data associated with this study will be made available upon

reasonable request.

#### CRediT authorship contribution statement

M.H. Shahini: Writing – original draft, Methodology, Investigation, Formal analysis, Data curation. Ali Kaveh: Writing – original draft, Software, Methodology, Investigation, Formal analysis, Data curation. Bin Zhang: Software, Methodology, Investigation, Formal analysis, Data curation. Hamed Ghadimi: Software. S. Guo: Funding acquisition. C. Zeng: Resources. W.J. Meng: Writing – review & editing, Writing – original draft, Project administration, Methodology, Investigation, Funding acquisition, Formal analysis, Data curation, Conceptualization.

### Declaration of competing interest

The authors declare that they have no known competing financial interests or personal relationships that could have appeared to influence the work reported in this paper.

# Data availability

Data will be made available on request.

# Acknowledgements

This work was funded in part by the NSF EPSCoR program under awards OIA-2118756 and OIA-1946231, and the Louisiana Board of Regents. The use of experimental facilities at the LSU Shared Instrumentation Facility (SIF), a part of the Louisiana Core User Facilities (CUF), is acknowledged. WJM acknowledges helpful discussions with Profs. J.W. Hutchinson and A. Needleman with thanks.

## References

- W.E. Frazier, Metal additive manufacturing: a review, J. Mater. Eng. Perform. 23 (2014) 1917–1928.
- [2] A. Vafadar, F. Guzzomi, A. Rassau, K. Hayward, Advances in metal additive manufacturing: a review of common processes, industrial applications, and current challenges, Appl. Sci. 11 (2021) 1213/1–121331.
- [3] F.H. Kim, S.P. Moylan, Literature Review of Metal Additive Manufacturing Defects, NIST Advanced Manufacturing Series, 2018, pp. 100–116, https://doi.org/ 10.6028/NIST.AMS.100-16.
- [4] K.S. Chan, M. Koike, R.L. Mason, T. Okabe, Fatigue life of Titanium alloys fabricated by additive layer manufacturing techniques for dental implants, Metall. Mater. Trans. A44 (2013) 1010–1022.
- [5] P. Li, D.H. Warner, A. Fatemi, N. Phan, Critical assessment of the fatigue performance of additively manufactured Ti–6Al–4V and perspective for future research, Int. J. Fatig. 85 (2016) 130–143.
- [6] P. Edwards, M. Ramulu, Fatigue performance evaluation of selective laser melted Ti-6Al-4V, Mater. Sci. Eng. A598 (2014) 327–337.
- [7] J.N. Domfang Ngnekou, Y. Nadot, G. Henaff, J. Nicolai, W.H. Kan, J.M. Cairney, L. Ridosz, Fatigue properties of AlSi10Mg produced by additive layer manufacturing, Int. J. Fatig. 119 (2019) 160–172.
- [8] S. Beretta, S. Romano, A comparison of fatigue strength sensitivity to defects for materials manufactured by AM or traditional processes, Int. J. Fatig. 94 (2017) 178–191.
- [9] S. Liu, Y.C. Shin, Additive manufacturing of Ti6Al4V alloy: a review, Mater. Des. 164 (2019) 107552.
- [10] S. Romano, A. Bruckner-Foit, A. Brandao, J. Gumpinger, T. Ghidini, S. Beretta, Fatigue properties of AlSi10Mg obtained by additive manufacturing: defect-based modelling and prediction of fatigue strength, Eng. Fract. Mech. 187 (2018) 165–189.
- [11] Y. Kok, X.P. Tan, P. Wang, M.L.S. Nai, N.H. Loh, E. Liu, S.B. Tor, Anisotropy and heterogeneity of microstructure and mechanical properties in metal additive manufacturing: a critical review. Mater. Des. 139 (2018) 565–586.
- [12] A. Yadollahi, N. Shamsaei, Additive manufacturing of fatigue resistant materials: challenges and opportunities, Int. J. Fatig. 98 (2017) 14–31.
- [13] ASTM E466 15, Standard Practice for Conducting Force Controlled Constant Amplitude Axial Fatigue Tests of Metallic Materials. ASTM International, 2015.
- [14] ASTM E647 23, Standard Test Method for Measurement of Fatigue Crack Growth Rates, ASTM International, 2023.
- [15] Y. Yamashita, T. Murakami, R. Mihara, M. Okada, Y. Murakami, Defect analysis and fatigue design basis for Ni-based superalloy 718 manufactured by selective laser melting, Int. J. Fatig. 117 (2018) 485–495.

- [16] A. Yadollahi, M.J. Mahtabi, A. Khalili, H.R. Doude, J.C. Newman Jr., Fatigue life prediction of additively manufactured material: effects of surface roughness, defect size, and shape, Fatig. Fract. Eng. Mater. Struct. 41 (2018) 1602–1614.
- [17] P. Fernandez-Zelaia, J.O. Rojas, J. Ferguson, S. Dryepondt, M.M. Kirka, Fatigue crack growth resistance of a mesoscale composite microstructure Haynes 282 fabricated via electron beam melting additive manufacturing, J. Mater. Sci. 57 (2022) 9866–9884.
- [18] S. Kalpakjian, S.R. Schmid, Manufacturing Processes for Engineering Materials, fifth ed., Prentice Hall, 2008.
- [19] C.A. Volkert, A.M. Minor, Focused ion beam microscopy and micromachining, MRS Bull. 32 (2007) 389–395.
- [20] C. Jiang, H. Lu, H. Zhang, Y. Shen, Y. Lu, Recent advances on in situ SEM mechanical and electrical characterization of low-dimensional nanomaterials, Scanning (2017) 1985149/1–198514911.
- [21] M.D. Uchic, D.M. Dimiduk, J.N. Florando, W.D. Nix, Sample dimensions influence strength and crystal plasticity, Science 305 (2004) 986–989.
- [22] J.R. Greer, J.Y. Kim, M.J. Burek, The in-situ mechanical testing of nanoscale single crystalline nanopillars, J. Miner. Met. Mater. Soc. 61 (12) (2009) 19–25.
- [23] J. Gong, A.J. Wilkinson, Anisotropy in the plastic flow properties of single-crystal α titanium determined from micro-cantilever beams, Acta Mater. 57 (2009) 5603–5705
- [24] D. Kiener, C. Motz, G. Dehm, R. Pippan, Overview on established and novel FIB based miniaturized mechanical testing using in-situ SEM, Int, J. Math. Res. 100/8 (2009) 1074–1087.
- [25] J. Ast, M. Ghidelli, K. Durst, M. Goken, M. Sebastiani, A.M. Korsunsky, A review of experimental approaches to fracture toughness evaluation at the micro-scale, Mater. Des. 173 (2019) 107762/1–10776224.

- [26] B. Zhang, H. Ding, A.C. Meng, S. Nemati, S. Guo, W.J. Meng, Crack reduction in Inconel 939 with Si addition processed by laser powder bed fusion additive manufacturing, Addit. Manuf. 72 (2023) 103623/1–10362315.
- [27] H. Wen, C. Zeng, A.H. Ettefagh, J. Gao, S. Guo, Laser surface treatment of Ti-10Mo alloy under Ar and N2 environment for biomedical application, J. Laser Appl. 31 (2019), 022012/1-9.
- [28] H. Wen, Laser surface treatment and laser powder bed fusion additive manufacturing study using custom designed 3D printer and the application of machine learning in materials science, LSU Doctoral Dissertations #5640, https://r epository.lsu.edu/gradschool\_dissertations/5640, 2021.
- [29] S. Suresh, Fatigue of Materials, second ed., Cambridge University Press, Cambridge, UK, 1998.
- [30] F. Iqbal, J. Ast, M. Goken, K. Durst, In situ micro-cantilever tests to study fracture properties of NiAl single crystals, Acta Mater. 60 (2012) 1193–1200.
- [31] W. Hoffelner, Fatigue crack growth in high temperature alloys, in: M. Gell (Ed.), Superalloys 1984: Proceedings of the Fifth International Symposium on Superalloys, Metallurgical Society of AIME, 1984, pp. 771–783.
- [32] K. Gruber, P. Szymczyk-Ziolkowska, S. Dziuba, S. Duda, P. Zielonka, S. Seitl, G. Lesiuk, Fatigue crack growth characterization of Inconel 718 after additive manufacturing by laser powder bed fusion and heat treatment, Int. J. Fatig. 166 (2023) 107287/1–10728713.
- [33] S. Ghorbanpour, S. Sahu, K. Deshmukh, E. Borisov, T. Riemslag, E. Reinton, V. Bertolo, Q. Jiang, A. Popovich, A. Shamshurin, M. Knezevic, V. Popovich, Effect of microstructure induced anisotropy on fatigue behaviour of functionally graded Inconel 718 fabricated by additive manufacturing, Mater. Char. 179 (2021) 111350/1–11135018.
- [34] D. Tabor, The Hardness of Metals, Oxford University Press, 1951.
- [35] V.S. Deshpande, A. Needleman, E. Van der Giessen, Discrete dislocation plasticity modeling of short cracks in single crystals, Acta Mater. 51 (2003) 1–15.